Supplementary Materials for

Structure of a human 48*S* translational initiation complex

Jailson Brito Querido*, Masaaki Sokabe*, Sebastian Kraatz*, Yuliya Gordiyenko, J. Mark Skehel, Christopher S. Fraser†, V. Ramakrishnan†

*These authors contributed equally to this work.
†Corresponding author. Email: csfraser@ucdavis.edu (C.S.F.); ramak@mrc-lmb.cam.ac.uk (V.R.)

Published 4 September 2020, *Science* **369**, 1220 (2020)
DOI: 10.1126/science.aba4904

This PDF file includes:

Other Supplementary Material for this manuscript includes the following:
(available at science.sciencemag.org/content/369/6508/1220/suppl/DC1)

MDAR Reproducibility Checklist (.pdf)
Movie S1 (.mp4)

Materials and Methods

Purification of human eIFs

Human initiation factors, ribosomes, capped mRNA, and $tRNA_i^{Met}$ for structural analysis were prepared as described previously (*12*, *47*, *50*). The eIF3c fragment (residues 1-165, 166-287, or 1-287) with N-terminal His- and MBP-tags and a TEV protease site was expressed in BL21 (DE3) cells at 30 °C for 4 hours. The protein was purified with nickel-nitrilo-triacetic acid agarose (Ni-NTA) resin (QIAgen), and subsequently passed over a Mono Q (5/5) column (GE Healthcare) and eluted using a 50-500 mM KCl gradient.

The C-terminal fluorescent-labelled eIF4A was prepared in a similar way as the C-terminal labelled eIF1 described previously (1), but using expressed protein ligation instead of amine-aldehyde coupling. Briefly, eIF4A was expressed in BL21 (DE3) as a C-terminal fusion with the C-His6-tagged Mxe GyrA intein. To increase the intein cleavage and labelling efficiency, the construct had a single phenylalanine residue inserted between the C-terminus of eIF4A and the intein. The protein was purified using Ni-NTA resin, and then cleaved by incubating with 0.5 M sodium 2-mercaptoethanesulfonate (MESNA) overnight at 4 °C, yielding ~ 70% cleavage. The protein was precipitated and washed with 3 M ammonium sulfate to remove excess MESNA, resuspended and passed through Ni-NTA resin again to remove the uncleaved protein and cleaved intein. The protein was further purified with Q Sepharose resin (GE Healthcare) in a buffer supplemented with 10 mM MESNA, and step-wise eluted with 400 mM KCl buffer. The resulting eIF4A-MESNA (2.5 nmol) was ligated with 1 mM NH2-Cys-Lys-COOH dipeptide modified with 6-carboxyfluorescein at the side chain amine of lysine in the presence of 0.4 M 4-Mercaptophenylacetic acid, 10 mM tris(2-carboxyethyl)phosphine (TCEP), 200 mM Hepes.KOH pH 7.0, and 200 mM KCl in 50 µl reaction. The mixture was incubated overnight at 4 °C, yielding > 80% labelling efficiency. Free dipeptide was removed by repetitive dilution and concentration using Amicon Ultra (Millipore) until absorbance of the flowthrough reached an undetectable level.

Functional analysis of the complex by ReIE assay

For the RelE assay, capped RNAs were modified with fluorescein at the 3'-end as previously described (*12*). A plasmid expressing RelB-RelE was a gift from Prof. Strobel in Yale University. RelE protein was expressed and purified as previously described (*51*). RelE assay was done essentially as described previously (*11*). For better quantification, mRNA cleavages were directly detected by gel imaging of 3'-end fluorescent RNA fragments instead of using reverse transcription with radioactive nucleotides. The 43S PIC (500 nM eIF1/1A/3j/5, 300 nM eIF2, 350 nM Met-$tRNA_i$, 200 µM GMPPNP, 250 nM eIF3, and 200 nM 40S subunit) in buffer A (20 mM tris-acetate pH 7.5, 70 mM KCl, 2.5 mM $MgCl_2$, 0.1 mM spermidine, 1 mM DTT, and 10% glycerol) was preincubated for 10 min at 37 °C in the presence or absence of eIF4F/4B (500 nM eIF4A/4B/4E, and 400 nM eIF4G (residue 557-1599)). The reaction was initiated by adding 50 nM labeled RNA together with 0.5 mM ATP-Mg or its analog, and was further incubated at 37 °C. At each time point, 8 µl reaction was withdrawn, and cleaved by 8 µM RelE in the presence of 2.5 µM competitor RNA (50-fold molar excess) to stop further recruitment of the substrate. The competitor RNA had a sequence identical to the substrate, but lacking fluorescent probe. After 10 min cleavage at 37 °C, the reaction was quenched by adding 10 µl of 10 M urea. The RNA was resolved by 10% polyacrylamide gel in 73 mM sodium-borate pH 8.1 buffer with 8 M urea, and imaged by LAS-4000 fluorescence image analyzer (GE Life Sciences). The amount of cleavage was quantified as a sum of cleavages at two AUGs, and was normalized to a total intensity of cleaved and uncleaved bands in each lane. The background cleavage (normally ~1%) was

measured by adding RelE and a competitor RNA together with the substrate RNA at time 0, and was subtracted from quantifications of kinetic measurements. RelE cleavage was absolutely dependent on both 40S and eIF2 ternary complex, and no cleavage at non-AUG codon was observed under the experimental condition (Fig. S1A).

MBP-pulldown assay

50 pmol of purified MBP tagged eIF3c (residues 1-287, 1-165, or 166-287) or MBP was mixed with 100 pmol of eIF1 in 50 µl reaction buffer containing 20 mM Hepes-K pH 7.5, 100 mM KCl, 2 mM MgCl2, 10% glycerol, 1 mM DTT, and 0.1% Nonidet P-40. The reaction mixture was incubated at 37 °C for 10 min. 50 µl of 40% amylose resin slurry (New England Biolab) in the reaction buffer was added and incubated on a rotator at 4 °C for 30 min. The resin was washed with 100 µl reaction buffer three times, and then boiled with 50 µl SDS gel loading buffer. The proteins were resolved on 15% SDS gel, and stained with Coomassie dye.

Fluorescence anisotropy assay

Fluorescence anisotropy assay was done essentially as described previously (*50*). Briefly, 20 nM fluorescent eIF4A was mixed with 0-700 nM eIF3 in the presence or absence of 1 µM eIF4G. We used the middle domain of eIF4G (residues 682-1104), a region that closely resembles the one we modeled in the structure. 20 µl reaction was incubated for 5 min at 37 °C, and further incubated for > 20 min at room temperature before measurement.

Reconstitution of human 48S pre-initiation complex for cryo-EM

48S complex was assembled by mixing 43S with eIF4F and eIF4B in a 50 µl reaction. The 43S was reconstituted by mixing 0.5 µM eIFs and 0.3 µM 40S, in buffer (97 mM KAc, 2.5 mM MgAc, 3% glycerol, 0.1 mM spermidine, 1mM DTT and 0.5 mM GMP-PNP) to a final volume of 26 µl. The reaction mix was incubated at 30 °C for 10 min. eIF4F was reconstituted by mixing 0.5 µM eIF4G (557-1599), 1 µM eIF4A, eIF4E, mRNA, and eIF4B, to a final volume of 24 µl, in the same buffer used to assemble the 43S, but supplemented with 0.5 mM ATP-γ -S instead of GMP-PNP.

Characterization of human 48S by SEC and western immunoblotting

For biochemical purpose only, a 48S complex was assembled as described for cryo-EM, in a buffer supplemented with 0.5 mM ATP-γ -S. The assembled complex was purified from free eIFs using size exclusion chromatography (SEC) as previously described (*52*). The protein composition of purified 48S was analysed by SDS-PAGE and stained with SYPRO Ruby (Bio-Rad). In parallel, proteins were also transferred to a nitrocellulose membrane (Bio-Rad). The membrane was incubated with primary antibodies against eIF4A (abcam, ab31217), eIF4E (abcam, ab33766), eIF4G (abcam, ab2609), eIF4B (abcam, ab186856) and the ribosomal protein eS24 (abcam, ab196652). Fluorescently-labelled secondary antibody conjugates were used to detect eIFs.

Characterization of eIF4F-eIF3 complexes by SEC followed by Cross-linking mass spectrometry (XL-MS)

eIF3-eIF4F complex was assembled by mixing 4 µM eIF4F with 2 µM eIF3. The reaction mix was incubated at 30 °C for 10 min and purified from free factors by SEC. Spermidine (a polyamine with quenching properties) was omitted from the reaction mix. Purified complexes were cross-linked with a 300-fold excess of the N-hydroxysuccinimide (NHS) ester disuccinimidyl dibutyric

urea (DSBU, ThermoScientific, USA), with respect to the protein concentration. The cross-linking reactions were incubated for 60 minutes at room temperature and then quenched by the addition of NH4HCO3 to a final concentration of 20 mM and incubated further for 15 min.

The cross-linked proteins were reduced with 10 mM DTT and alkylated with 50 mM iodoacetamide. Following alkylation, the proteins were digested with trypsin (Promega, UK) at an enzyme-to-substrate ratio of 1:100, for 1 hour at room temperature and then further digested overnight at 37 °C following a subsequent addition of trypsin at a ratio of 1:20.

The peptide digests were then fractionated batch wise by high pH reverse phase chromatography on micro spin C18 columns (Harvard Apparatus, USA), into four fractions (10 mM NH4HCO3 /10 % (v/v) acetonitrile pH 8, 10 mM NH4HCO3 /20 % (v/v) acetonitrile pH 8, 10 mM NH4HCO3 /40 % (v/v) acetonitrile pH 8 and 10 mM NH4HCO3 /80 % (v/v) acetonitrile pH 8. The 150 ul fractions were evaporated to dryness on a CoolSafe lyophilizer (ScanVac, Denmark) prior to analysis by LC-MS/MS.

Lyophilized peptides for LC-MS/MS were resuspended in 0.1 % (v/v) formic acid and 2 % (v/v) acetonitrile and analyzed by nano-scale capillary LC-MS/MS using an Ultimate U3000 HPLC (ThermoScientific Dionex, USA) to deliver a flow of approximately 300 nl/min. A C18 Acclaim PepMap100 5 µm, 100 µm × 20 mm nanoViper (ThermoScientific Dionex, USA), trapped the peptides before separation on a C18 Acclaim PepMap100 3 µm, 75 µm × 250 mm nanoViper (ThermoScientific Dionex, USA). Peptides were eluted with a gradient of acetonitrile. The analytical column outlet was directly interfaced via a nano-flow electrospray ionisation source, with a quadrupole Orbitrap mass spectrometer (Q-Exactive HFX, ThermoScientific, USA). MS data were acquired in data-dependent mode using a top 10 method, where ions with a precursor charge state of 1+ and 2+ were excluded. High-resolution full scans (R=120 000, m/z 300-1800) were recorded in the Orbitrap followed by higher energy collision dissociation (HCD) (stepped collision energy 26 and 28 % Normalized Collision Energy) of the 10 most intense MS peaks. The fragment ion spectra were acquired at a resolution of 50 000 and dynamic exclusion window of 20s was applied.
For data analysis, Xcalibur raw files were converted into the MGF format using Proteome Discoverer version 2.3 (ThermoScientific, USA) and used directly as input files for MeroX (*53*). Searches were performed against an ad hoc protein database containing the sequences of the proteins in the complex and a set of randomized decoy sequences generated by the software. The following parameters were set for the searches: maximum number of missed cleavages 3; targeted residues K, S, Y and T; minimum peptide length 5 amino acids; variable modifications: carbamidomethylation of cysteine (mass shift 57.02146 Da), Methionine oxidation (mass shift 15.99491 Da); DSBU modified fragments: 85.05276 Da and 111.03203 Da (precision: 5 ppm MS and 10 ppm MS/MS); False Discovery Rate cut-off: 5 %. Finally, each fragmentation spectrum was manually inspected and validated.

Cryo-EM grid preparation and data acquisition

To increase the occupancies of eIFs in the complex, the 48S was further stabilized by chemical crosslinking using 1.5 mM BS3 (final concentration) on ice for 30 min. 3 µl of 130 nM 48S complex (without any further purification step after the *in vitro* reconstitution) was applied onto

glow-discharged Quantifoil R2/2 copper grids pre-covered with thin layer of carbon (~20Å) made in-house. Cryo-EM grids were prepared using a FEI Vitrobot Mark IV at 4°C and 100% humidity. The grids were plunged into liquid ethane at 93 K in a precision cryostat system (*54*). Because the crosslinking reaction was performed on ice and in the presence of spermidine (a polyamine with quenching properties), as expected we observed a mild crosslinking effect, confirmed by the absence of aggregates in cryo-EM grids, when compared with the grids prepared without BS3.

Three independent data sets were collected on Titan Krios microscopes (ThermoFisher) equipped with Falcon III direct electron detector (FEI) at a magnification of 75,000x and at pixel sizes of 1.085 Åpix^{-1} (dataset 1 and 2) or 1.094 Åpix^{-1} (48S without eIF4B). 39 frames were collected for 1 s in linear mode with defoci ranging from -1.8 µm to -3.0 µm, and fluxes of 102-107 e/Å^2/s.

Image processing

Motion correction was performed using RELION 3's own implementation (*55*). Movies were aligned using 5×5 patches with dose-weighting. CTF was estimated using CTFFIND4 (*56*). The crystal structure of mammalian 40S (*57*) was used to simulate a map and used after lowpass filtering to 60 Å as a reference for the initial 3D classification. After focused classification on various regions of the map and 3D refinement, Bayesian polishing in RELION was used for beam-induced motion correction (*55*). The predominant molecular motions were accounted for by multi-body refinement and flexibility analysis in RELION (*58*). All reported resolutions are based on the gold-standard Fourier shell correlation (FSC) = 0.143 criterion (*59*).

Model building, fitting and refinement

The eIFs models were generated by SWISS-MODEL (*60*) using previous cryo-EM and crystal structures (*10*, *19*, *31*, *49*, *57*, *61–63*). Parts of some subunits, such as eIF3a, eIF3c, eIF3d, eIF3e and eIF3j were built *de novo*.

The model for the C-terminal domain of eIF3j was obtained by homology modelling using the crystal structure of human eIF3j (PDB: 3BPJ) and the main chain was further modelled by first predicting its secondary structure using PSIPRED (*64*). The main chain for the N-terminal domain was modelled based on the secondary structure prediction and refined into our map. The main chain for the low-resolution parts were modelled as poly-alanines.

eIF3g-RRM was modelled using the NMR structure of eIF3g (2CQ0) and further adjusted into our map in Coot.

eIF3c-NTD was built *de novo.*

The crystal structure of the partial eIF4G-eIF4A complex from yeast (*31*) was used to generate a homology models with the human sequences and fitted as a rigid body into the density.

Because the mRNA used lacks a start site, its structure in the channel is heterogenous. Thus, the model contains only the phosphate backbone. The 40S small ribosomal subunit was modelled based on a previous cryo-EM structure of human 80S (*65*). The high local resolution permitted *de novo* building and revealed chemical modifications previously reported in the human 80S (*65*).

Manual fitting and refinement was performed in Coot (*66*). Real space refinement was performed using phenix.real_space_refine (*67*).

40S and eIFs models were generated using cryo-EM maps obtained after multi-body refinement. Thus, each body was deposited with the corresponding map. To generate a global 48S, each model was rigid body fitted (using Chimera) into the density of global 48S obtained prior the multi-body

refinement. Three rounds of global optimization in phenix real space refinement and manual refinement in coot were also performed to improve the fit and remove clashes.

Figures and movie

Protein multiple sequence alignment was performed using the MPI Bioinformatics Toolkit (*68*). The figures were made in Chimera (*69*) and ChimeraX (*70*). The movie was made in PyMOL (Schrödinger).

The comparation between human 48S and previous structures of yeast 48S was performed by suppressing the two structures. 18S rRNA phosphate backbone was taken as a reference for structural alignments.

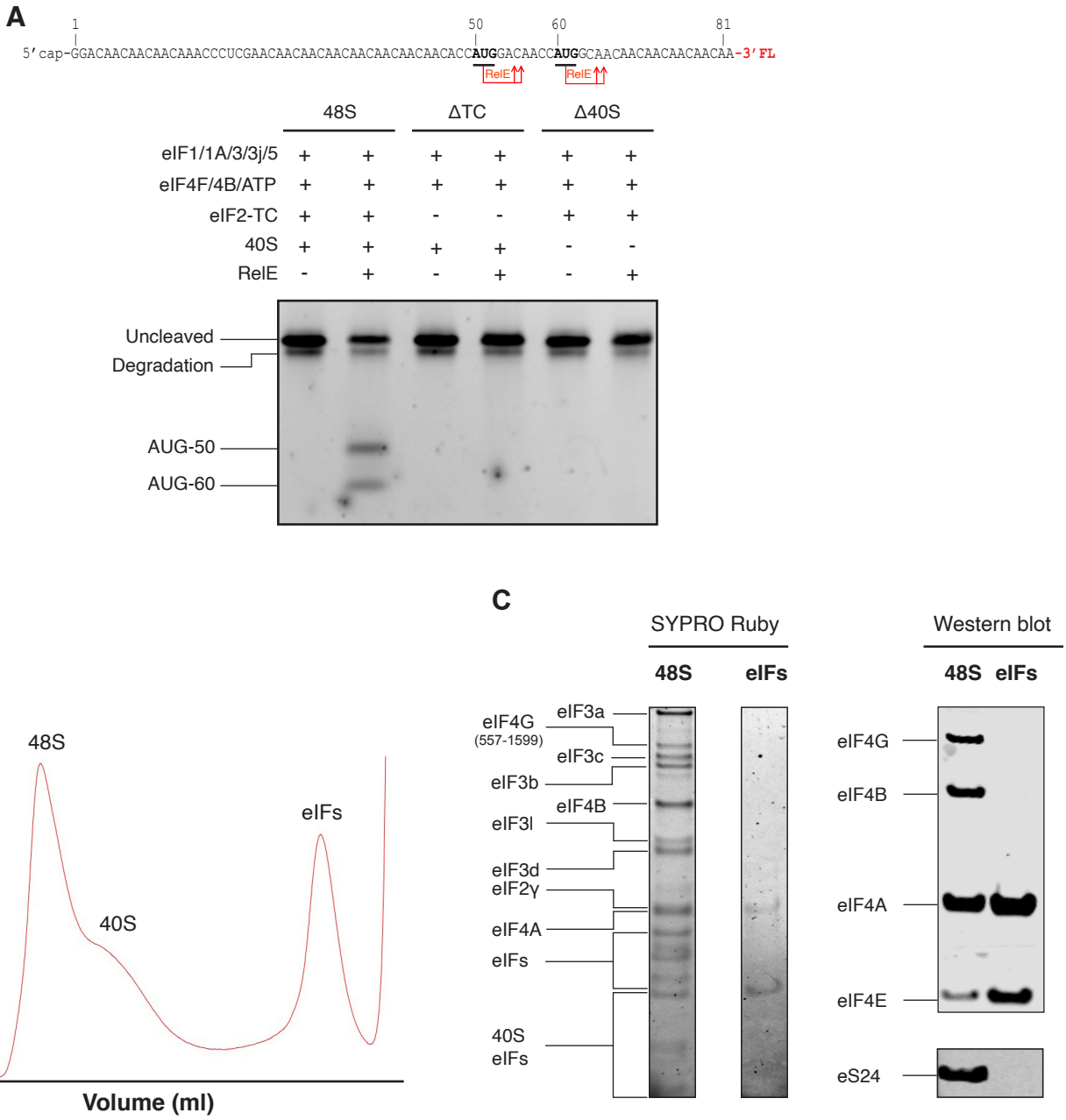

Figure S1: Analysis and characterization of human 48S. A) RelE cleavage shows that the efficiency of cleavage depends on both eIF2 ternary complex (lines 3 and 4) and 40S (lines 5 and 6). The RelE cleavage assay was performed for 40min at 37°C. **B)** Size exclusion chromatography (SEC) absorbance profile of a reconstituted 48S complex. The presence of free 40S subunits and unbound eIFs are also indicated. **C)** Biochemical characterization of the 48S complex and free eIFs fractions shown by SDS-PAGE analysis (left) or by western blot analysis for specific components (right).

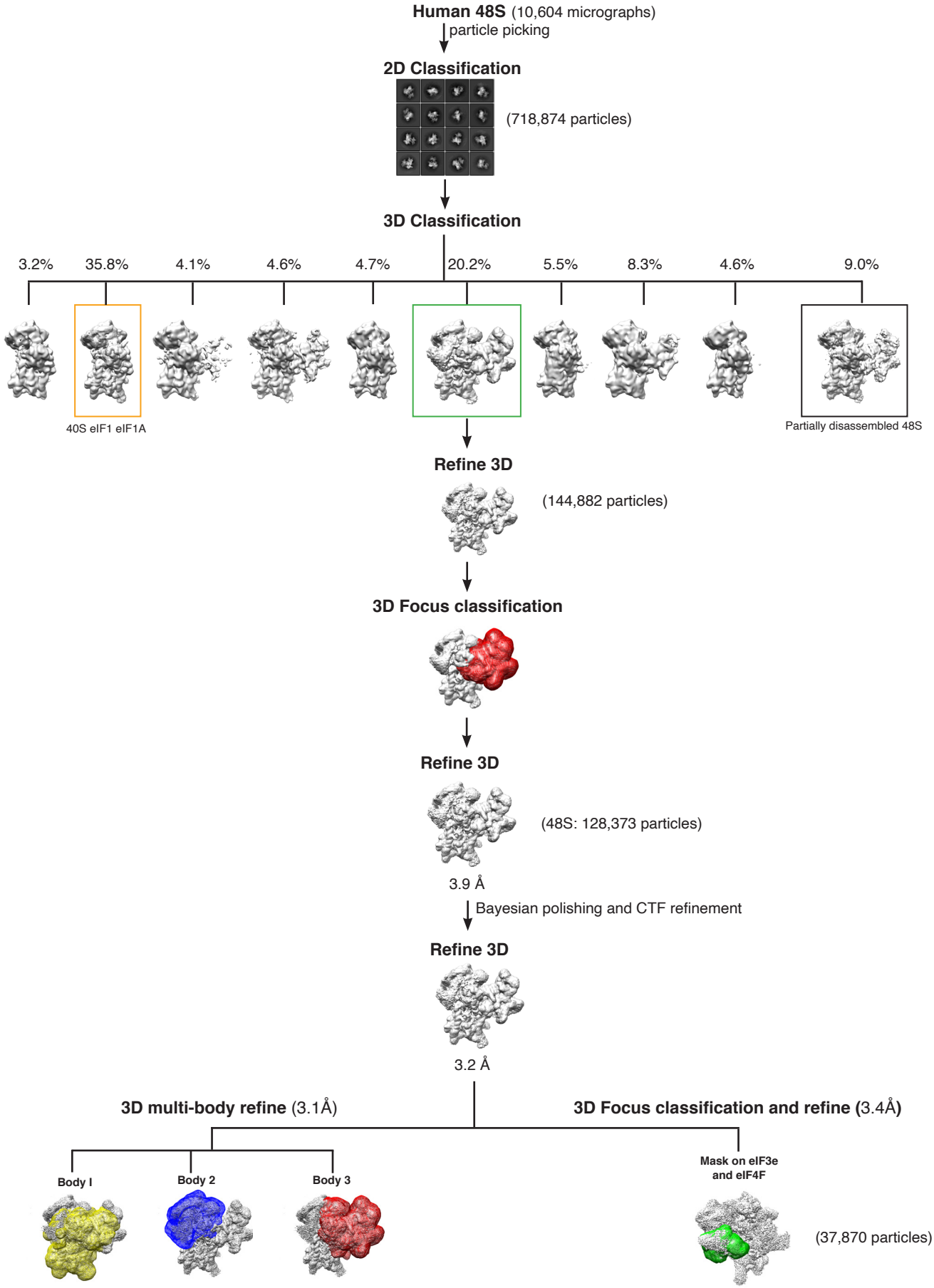

Figure S2: Cryo-EM analysis of human 48S. Data processing scheme used for structure determination of BS3 crosslinked 48S is shown. The main class (35.8%) correspond to 40S-eIF1-eIF1A particles. 20.2% of the particles are 48S and contain density for all 13 subunits of eIF3. Further 3D focus classification with signal subtraction was undertaken. 29.5% of 48S contain the additional density for eIF4F.

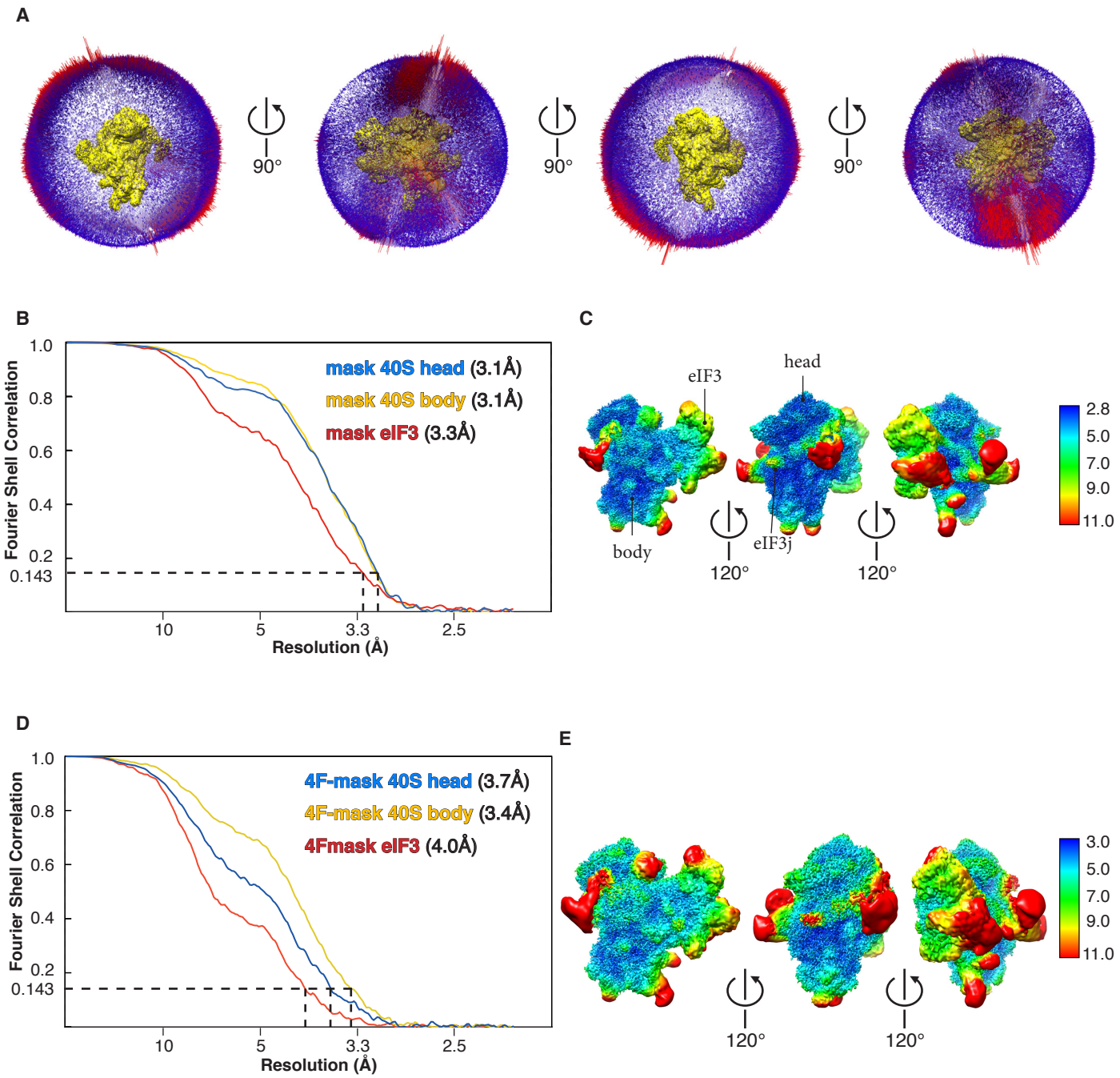

Figure S3: Particles distribution and resolution. A) Angular distribution plot of human 48S. **B-C)** Fourier shell correlation (FSC) curve and local resolution of the 48S after multi-body refinement. **D-E)** Fourier shell correlation (FSC) curve and local resolution of the 48S after 3D focus classification on eIF4F and multi-body refinement.

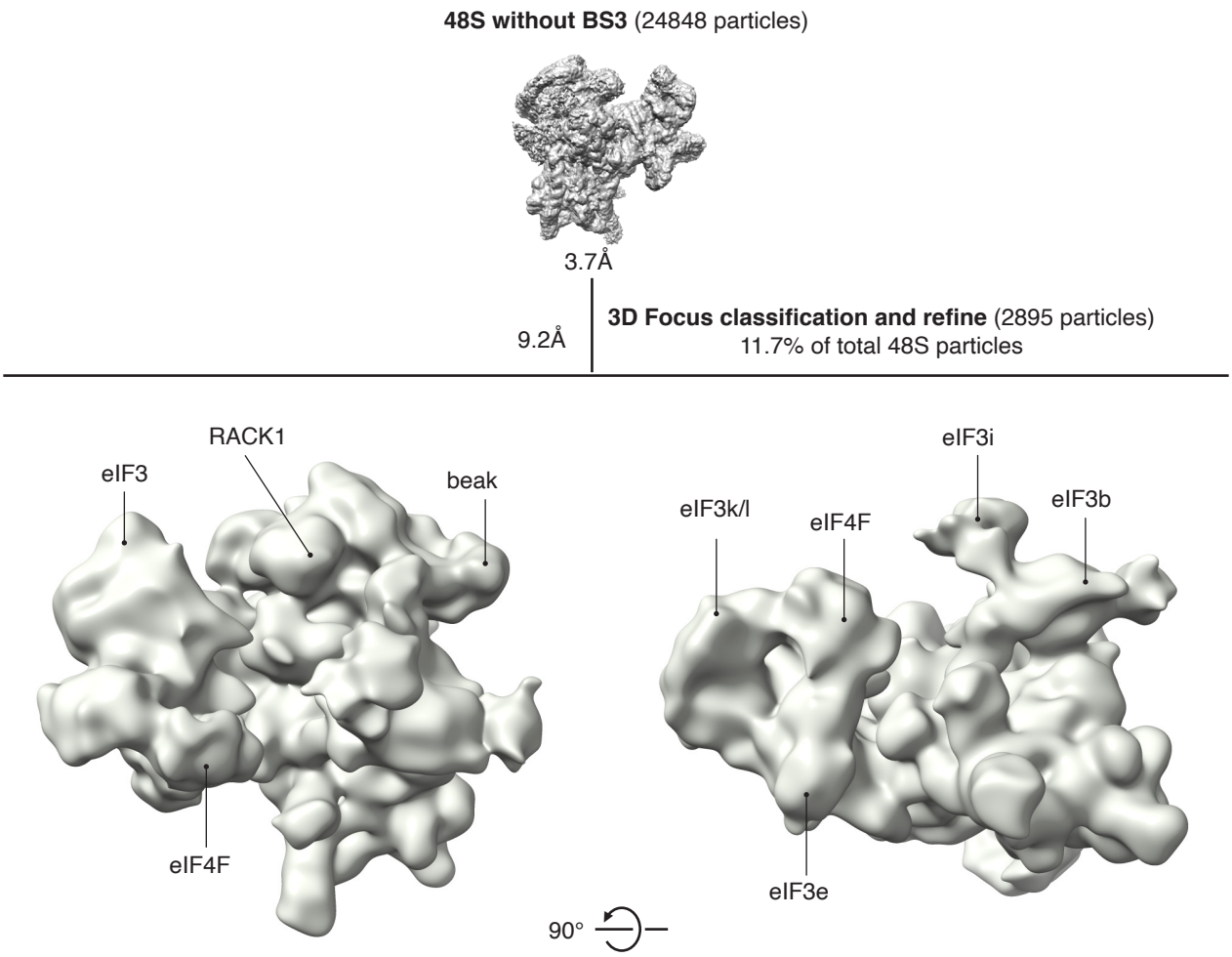

Figure S4: Cryo-EM reconstruction of human 48S obtained without BS3 crosslinking. 3D focus classification and refinement is shown for the 48S. Labels are shown for major regions of the 48S. eIF4F density is observed in the same location described in the sample stabilized with BS3 crosslinker.

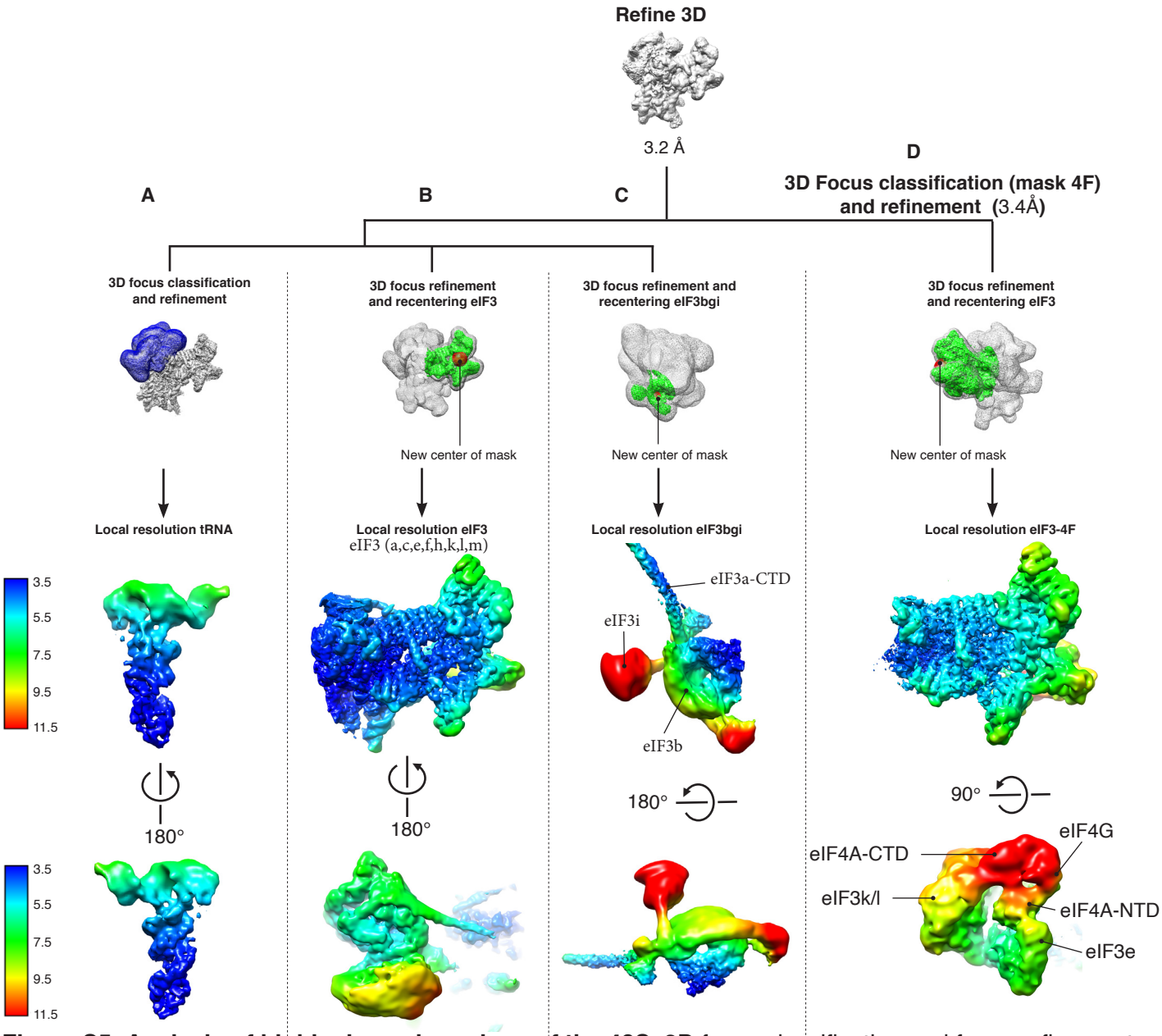

Figure S5: Analysis of highly dynamic regions of the 48S. 3D focus classification and focus refinements are shown for the head and eIF2-TC **(A)**, the eIF3 structural core **(B)**, the eIF3bgi subcomplex **(C)**, and the eIF3-eIF4F interaction.

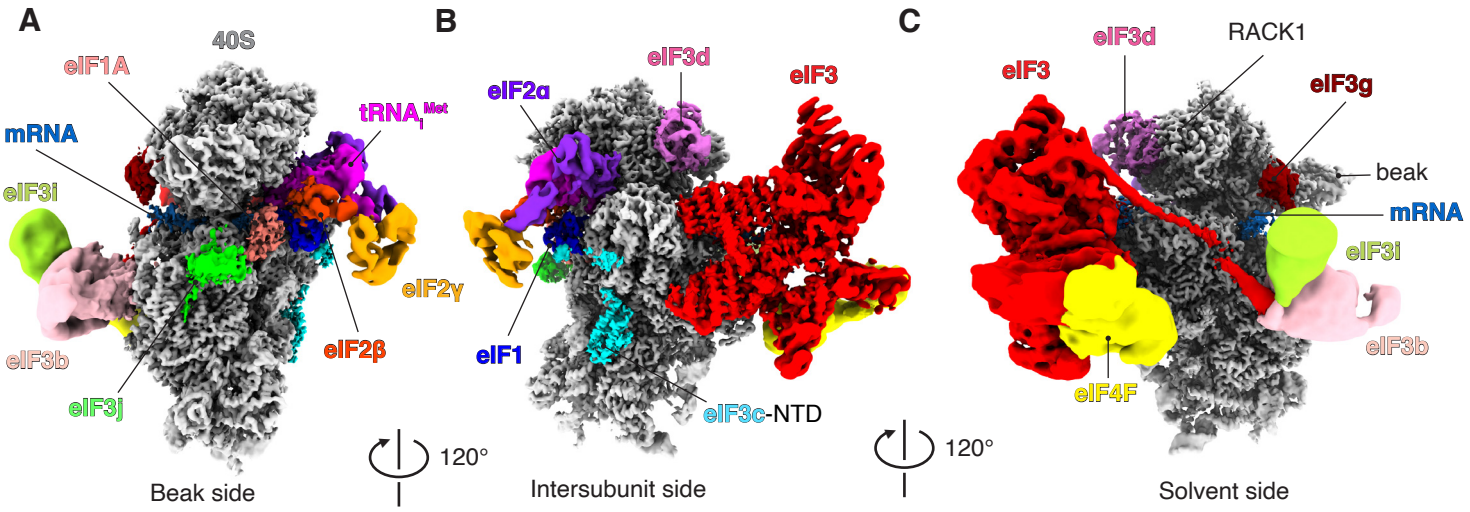

Figure S6: Cryo-EM reconstruction of human 48S. A-C) Segmented map filtered at local resolution. The segmented map is shown in three different orientations, as labelled. 40S is coloured in light-grey, eIF3 octameric structural core in red and eIF4F in yellow. Other 48S components are labelled accordingly.

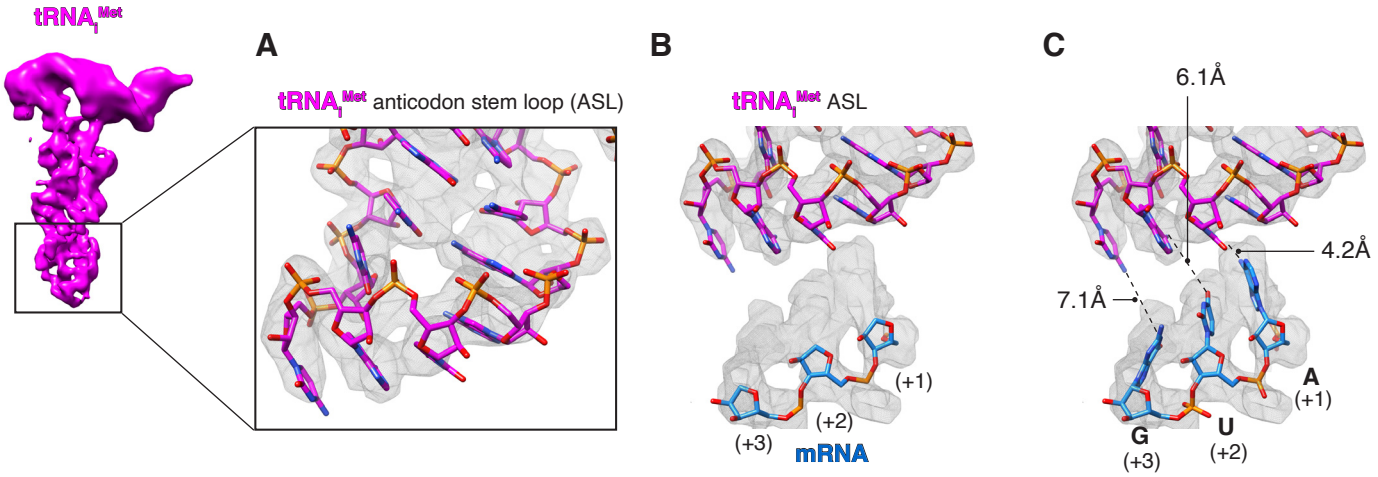

Figure S7: Views of the tRNA in the cryo-EM map. A) Map-to-model fts of tRNA$_i^{Met}$ anticodon stem loop (ASL). **B)** Close-up view of the P site to highlight the position of the anticodon and the unassigned density for the mRNA bases. The distribution of the mRNA is heterogenous, so only the sugar phosphate backbone is modelled. **C)** Modelling of bases for an AUG codon into the P site density shows that the distance between the bases are not compatible with hydrogen bond distances required for base pairing. It is important to highlight that the 48S structure was obtained using an mRNA lacking the start site.

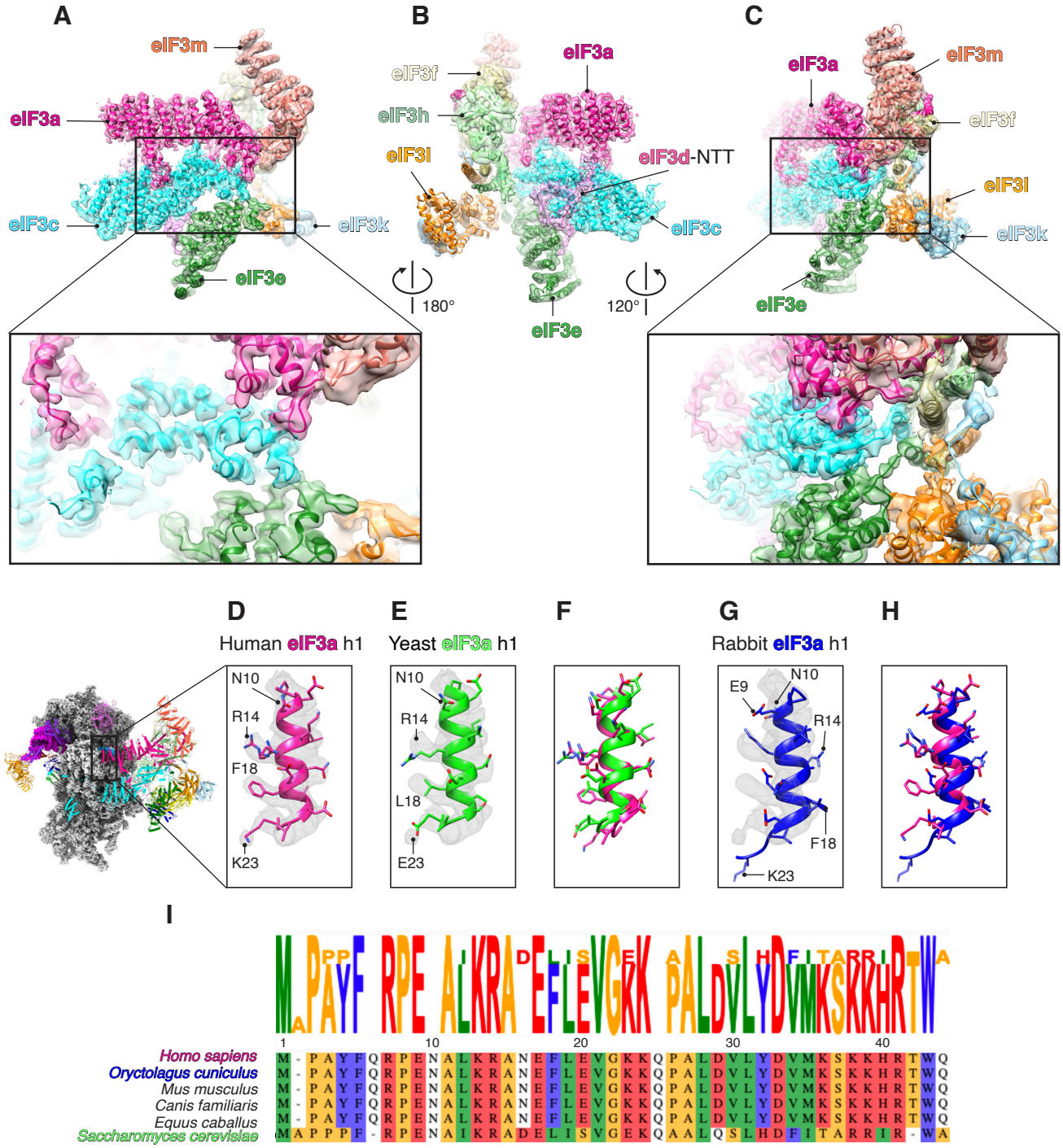

Figure S8: Structure of human eIF3 octameric structural core. A-C) Map-to-model fits of eIF3 octameric structural core to highligh the internal organization. **D)** Map-to-model fits of eIF3a helix 1 involved in the interaction with ribosomal protein eS1. **E)** Rigid-body fitting of yeast (*S. cerevisiae*) crystal structure of eIF3a helix 1 *(19)* into human cryo-EM map. **F)** Superposition of eIF3a structures shows structural conservation between human and yeast. **G)** Rigid-body fitting of a structure of rabbit eIF3a helix 1 *(10)* into human cryo-EM map. **H)** Superposition of eIF3a structures reveals the differences between human and low-resolution structure of rabbit eIF3a. In rabbit, all residues involved in the interaction with ribosomal protein eS1 are placed between 90° to 180° away from the human structure. **I)** Multiple sequence alignment of eIF3a N-terminal domain highlighting evolutionary conservation. The region involved in the interaction with ribosomal protein eS1 is 100% conserved in mammals. Low resolution data can explain the structural differences between human and rabbit eIF3a.

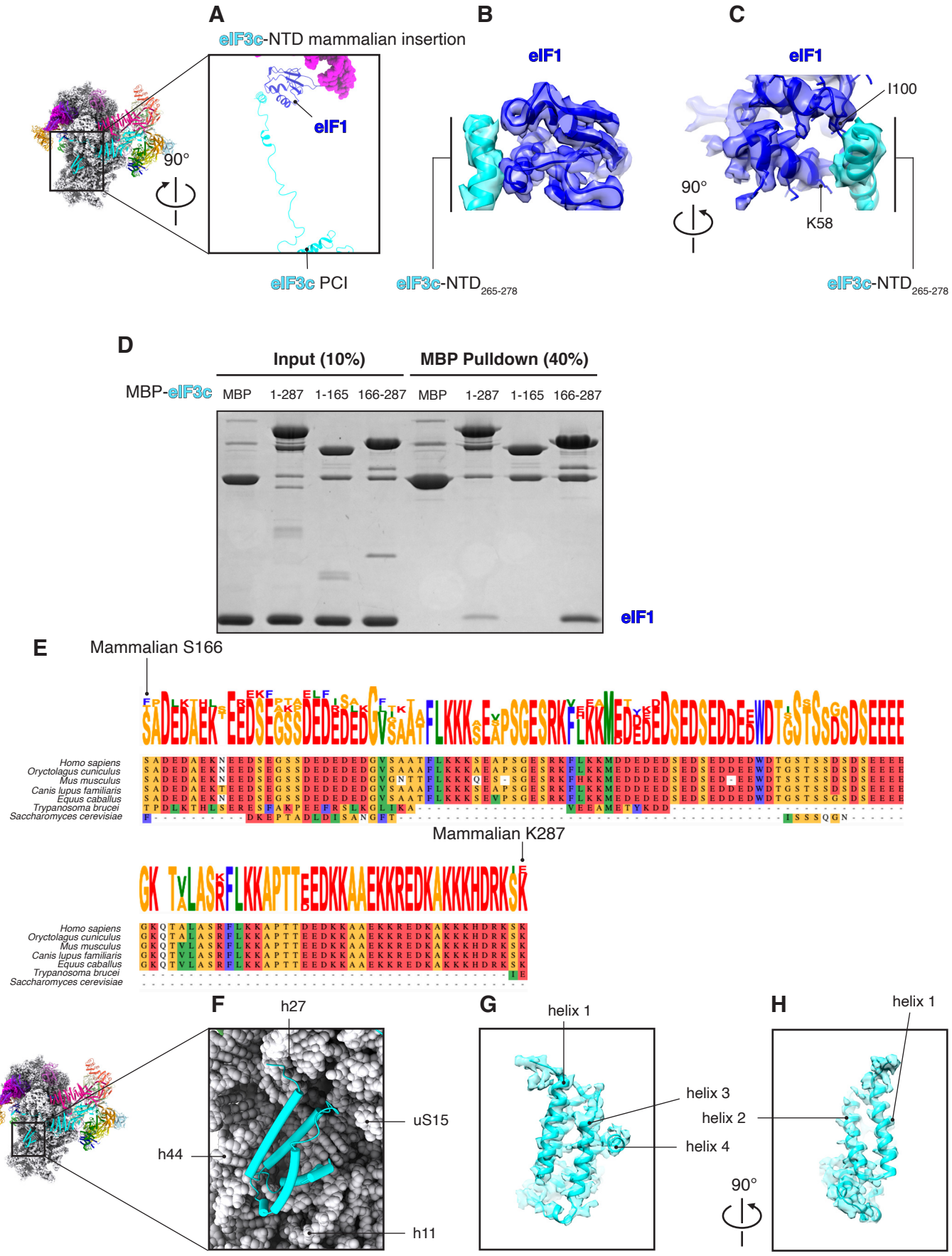

Figure S9: Interaction of human eIF3c N-terminal domain with 40S and eIF1. A) A mammalian conserved sequence insertion within eIF3c N-terminal domain extends from the eIF3 core towards the platform of the 40S where it interacts with eIF1 **(B, C)**. **D)** Immunoprecipitation of purified human eIF1 by purified maltose binding protein (MBP)-tagged eIF3c-NTD was carried out as described in materials and methods. eIF1 co-immunoprecipitates with eIF3c truncations that include the mammalian conserved insertion (eIF3c1-287 and eIF3c166-287). **E)** Multiple sequence alignment of the eIF3c N-terminal domain from different species. The mammalian conserved insertion is shown for residues 166-287. **F-H)** eIF3c-NTD cluster of helices ($eIF3c_{48-148}$) binds in a pocket formed by 18S rRNA h11, h27, h44 and r-protein uS15.

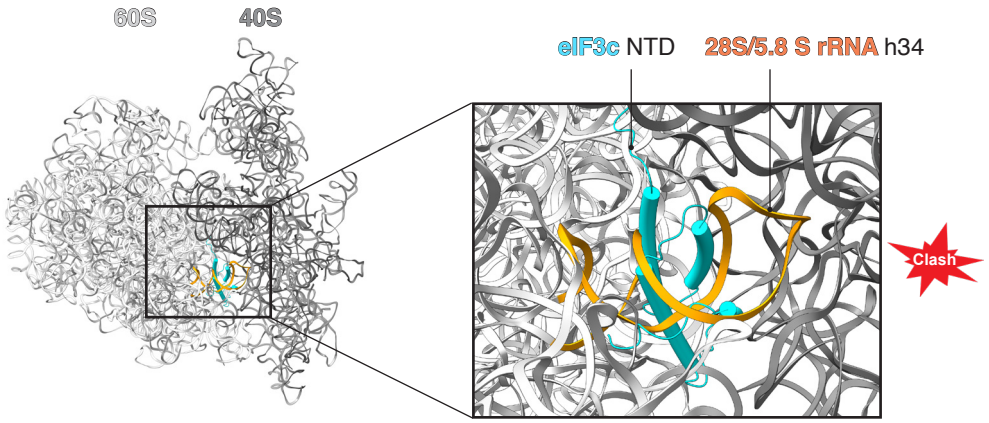

Figure S10: Superposition of eIF3c-NTD with human 80S ribosome. Superposition of the eIF3c-NTD cluster of four helices ($eIF3c_{48-148}$) with the structure of human 80S *(65)*. The eIF3c-NTD would clash with rRNA h34 from the large subunit, which is known to form a bridge contact between ribosomal subunits.

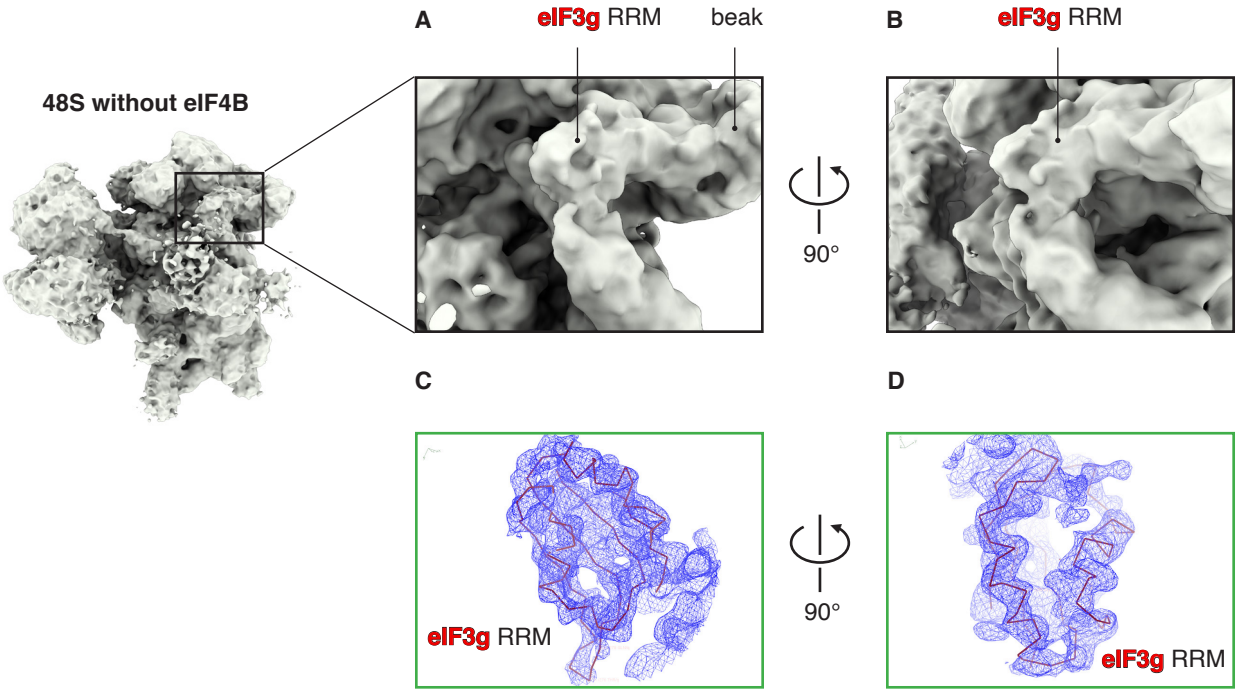

Figure S11: Cryo-EM reconstruction of human 48S assembled in the absence of eIF4B. A-B) Structure of eIF3g-RRM in a 48S assembled without eIF4B shown in two different views. **C-D)** Map-to-model fits of eIF3g-RRM.

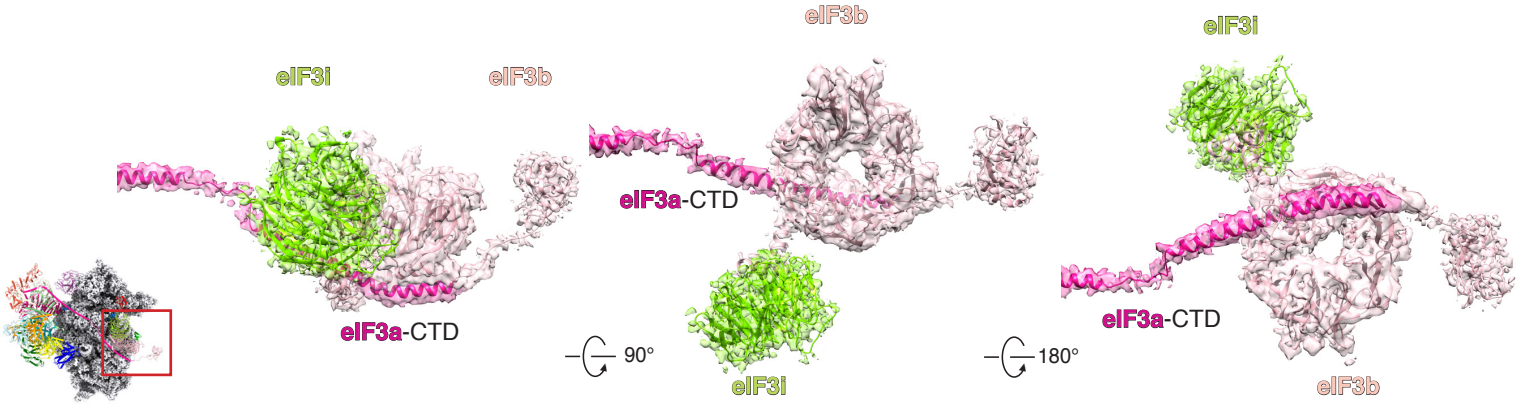

Figure S12: Structure of eIF3bgi subcomplex. A) Fits of eIF3bgi into the cryo-EM map. The structure of eIF3b and eIF3i were generated using the crystal structure of yeast eIF3bi *(19)*. The The polyalanine model of eIF3a-CTD was generated using and secondary-structure prediction provided by PSIPRED.

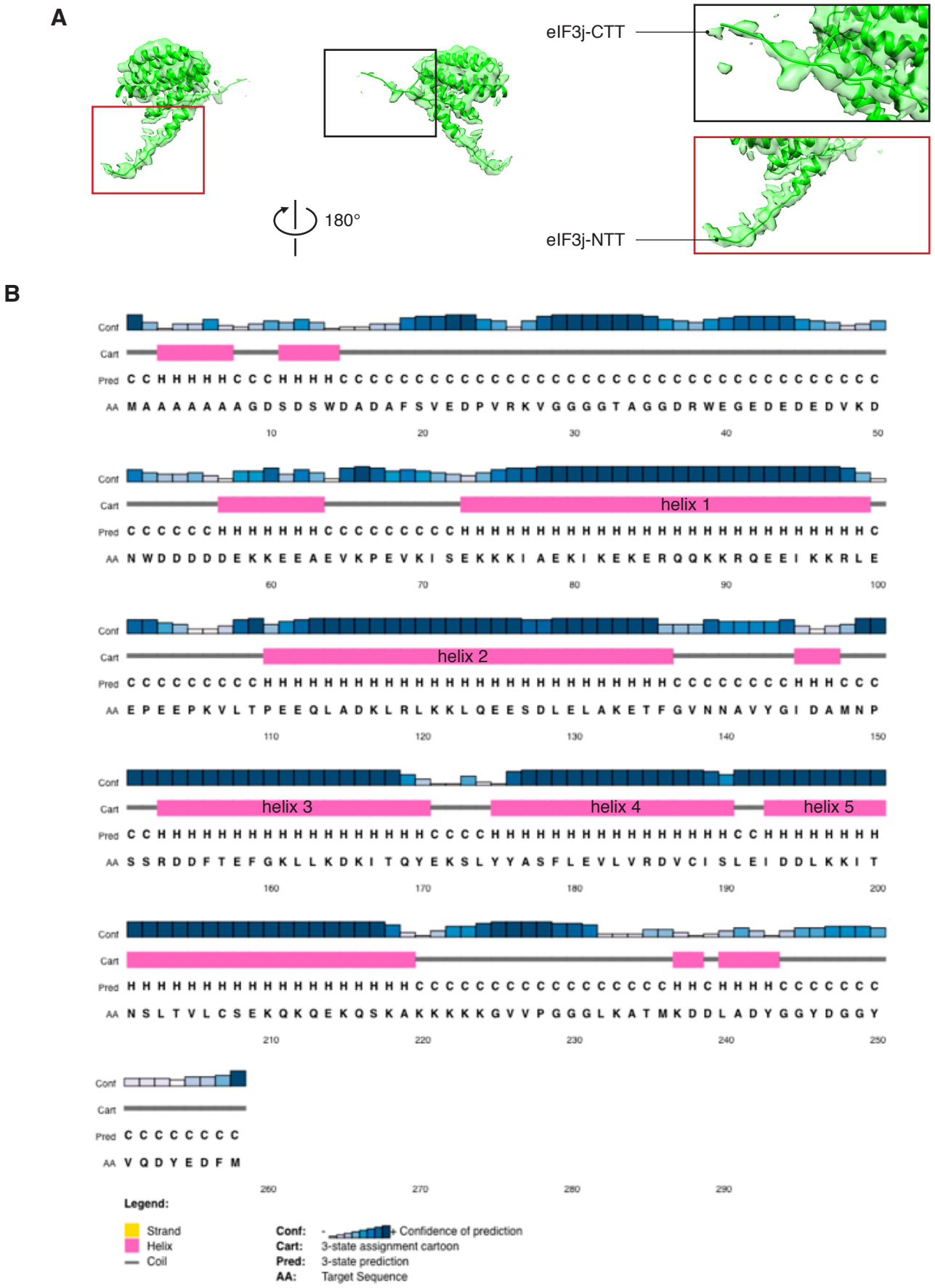

Figure S13: Structure of eIF3j. A) Fits of eIF3j into the cryo-EM map filtered at local resolution (4-9Å). The polyalanine model was generated using the crystal structure of human eIF3j (PDB:3BPJ) (helix 3-5) and secondary-structure prediction (helix 1-2) provided by PSIPRED **(B)**.

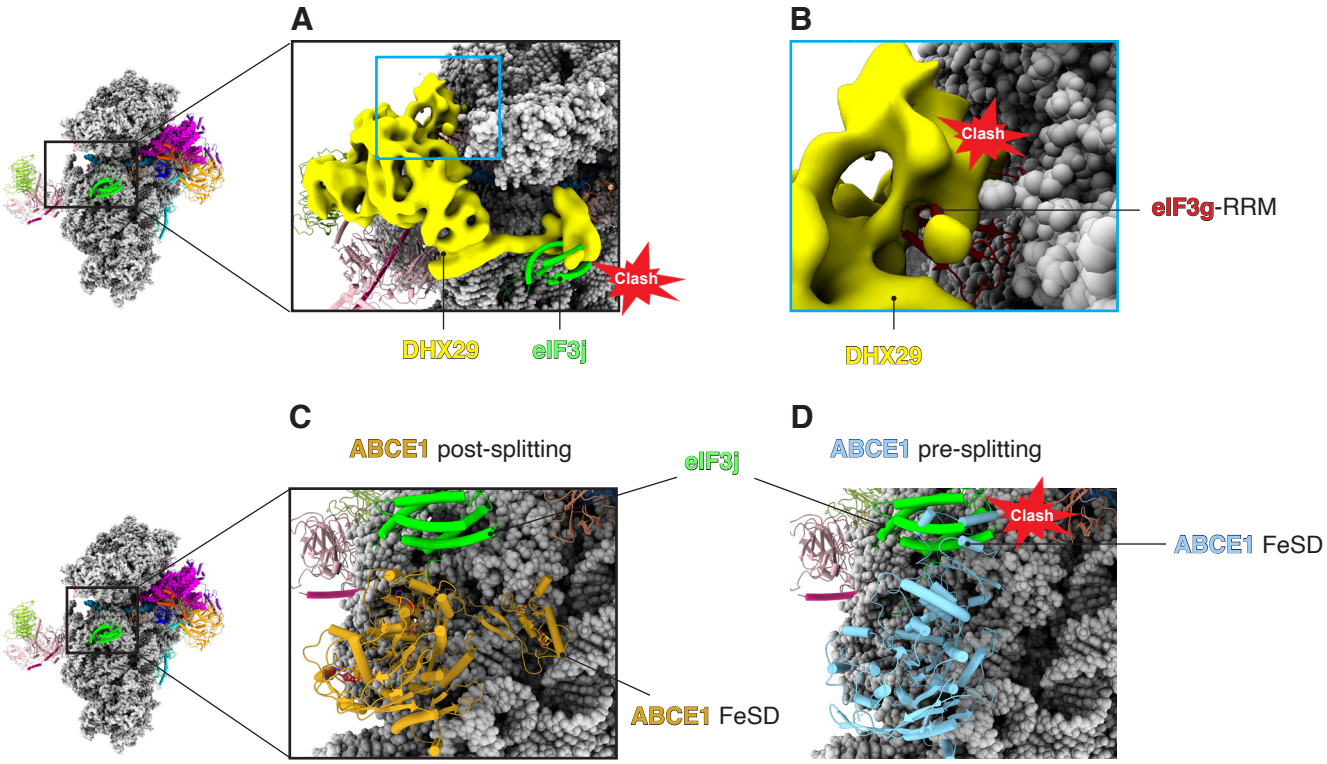

Figure S14: Superposition of eIF3j with the structure of ABCE1. A) Superposition of eIF3j in the 48S with the structure of DHX29 bound to the 43S PIC *(10)*. The position of DHX29 clashes with eIF3j as well as with the eIF3g-RRM **(B)**. **C)** Superposition of eIF3j in the 48S with the "post-splitting" structure of ABCE1 bound the 40S subunit *(29)*. D) Superposition of eIF3j with the "pre-splitting" structure of ABCE1 bound to the 80S ribosome *(71-72)*. A predicted steric clash between eIF3j and the iron–sulfur cluster domain (FeSD) in ABCE1 is labelled.

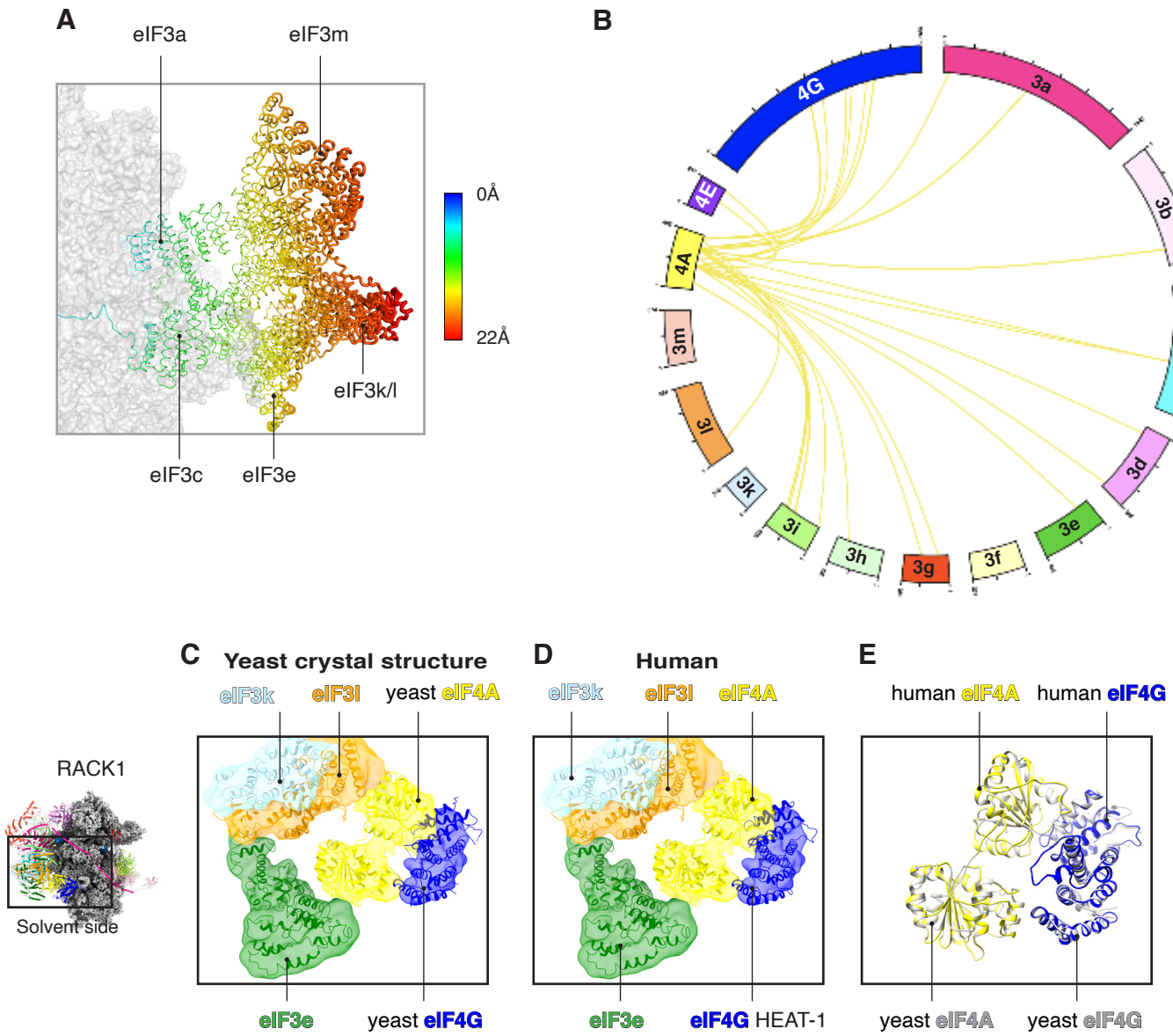

Figure S15: eIF4F binding to the eIF3 complex. A) Multi-body refinement and principal component were used to analyse the flexibility of eIF3 octameric structural core by measuring the relative positions of eIF3 and 40S. The eIF3k/l subunits are the most flexible region. **B)** A summary of crosslinking mass spectrometry of the eIF4F-eIF3 complex (match score: min 180; max 230), as described in materials and methods. Connecting lines between eIF4A and other proteins reflect the number of crosslinks observed. The majority of crosslinks are observed between eIF4A and the eIF3 structural core. **C)** Rigid-body fitting (correlation = 0.92) of *S. cerevisiae* crystal structure (31) into human cryo-EM map to local resolution (6-11Å). Yeast crystal structure (eIF4A seq Identity 67.40%; eIF4G-HEAT1 seq Identity 34.98%) was used for the homology model of human eIF4A-eIF4G. **D)** Rigid-body fitting of human homology model into the cryo-EM map. **E**) Superposition of human and yeast eIF4F.

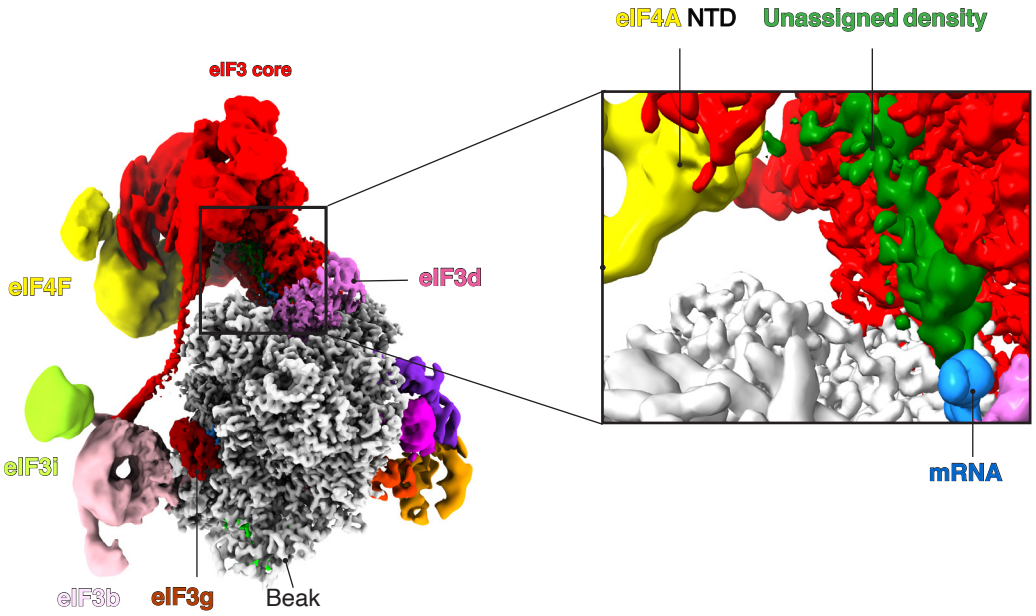

Figure S16: Cryo-EM reconstruction of human 48S. An unassigned density connects the mRNA (-14) with eIF4A.

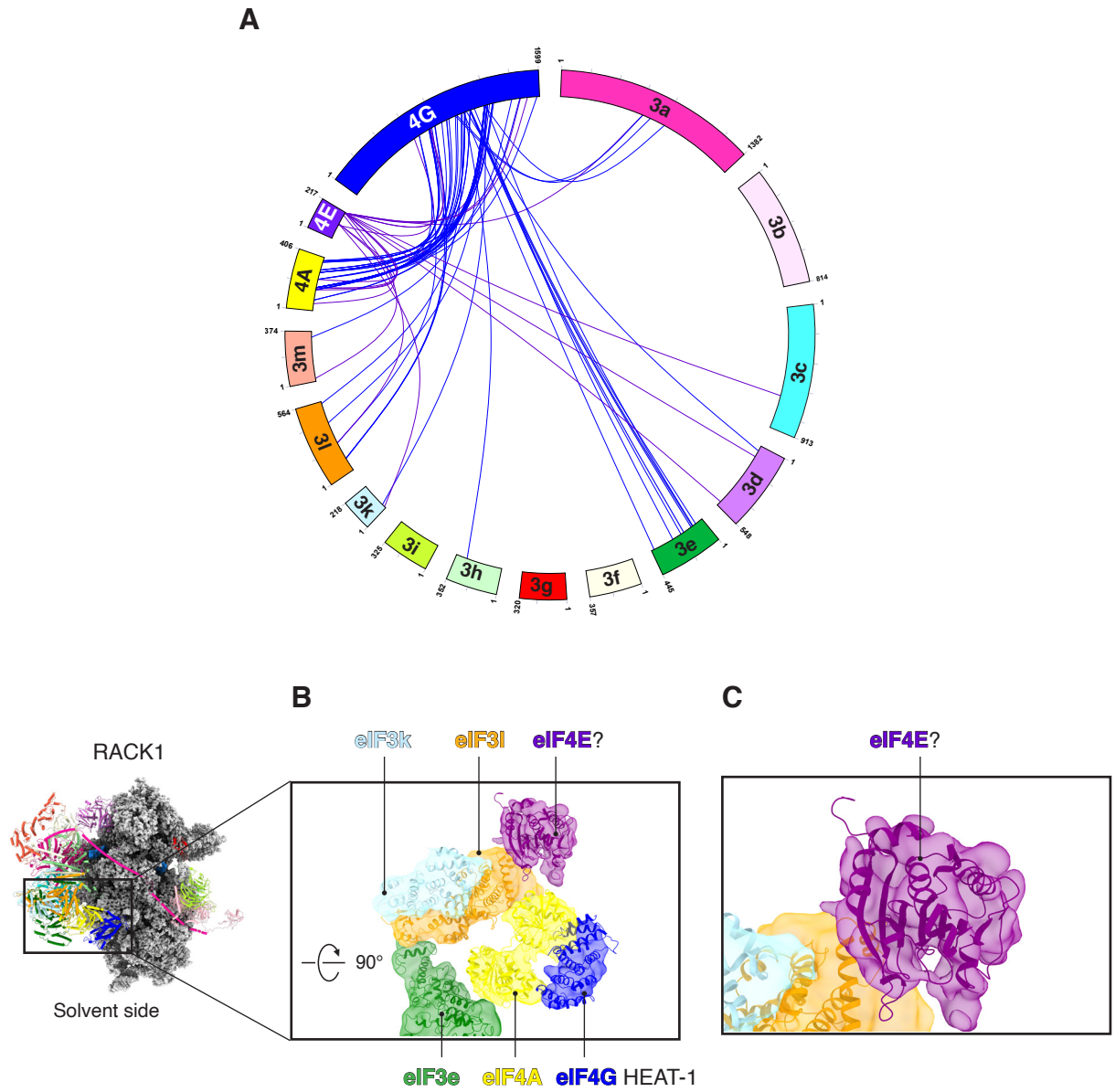

Figure S17: Fitting and density assignment to eIF4E. A) Crosslinking mass spectrometry of eIF4F-eIF3 complex revealed the interaction of eIF4E and eIF4G with the eIF3 structural core (match score: min 90; max 230), as described in materials and methods. **B-C)** Additional unassigned density is shown in proximity to the density we have assigned to eIF4A-eIF4G. Rigid-body fitting (correlation = 0.70) of the human crystal structure of eIF4E *(73)* into the unassigned density.

Table S1: Data collection, processing, refinement and model statistics.

Data Collection						
Microscope	Titan Krios					
Voltage (kV)	300					
Corrected Magnification	129,000					
Pixel size (Å)	1.074					
Detector	Falcon III					
Defocus range (μm)	-1.8 to -3.0					
Defocus mean (μm)	-2.4					
Total electron exposure ($e^{-}Å^{-2}s^{-}$)	107					
Exposure rate ($e^{-}Å^{-2}frame^{-1}$)	2.74					
Data collection software	EPU					
Data Processing						
Independent data collections	2					
Useable micrographs	10,604					
Particles	718,874					
Final particles (48S)	128,373					
Map sharpening B-factor ($Å^2$)	-10					
Accuracy translations (pix) / rotations (°)	0.39 / 0.46°					
Resolution (Å)						
Unmasked (0.143 FSC)	4.20					
Masked (0.143 FSC)	3.08					
Local resolution range (Å)	11-2.8					
Model	**body**	**head**	**eIF3**	**TC**	**eIF3bgi**	**48S**
EMDB accession code	10775	10772	10769	10774	10773	11302
PDB accession code	6YBW	6YBS	6YBD	6YBV	6YBT	6ZMW
Model Composition						
Chains	29	18	19	5	3	57
Non-hydrogen atoms	52908	28732	30742	6731	5426	118158
Protein residues	3374	2330	4421	769	1026	11116
RNA bases	1254	501	0	78	0	1822
Refinement						
Software			phenix.real_space_refine			
Resolution (Å)	3.1	3.1	3.3	3.8	6.0	3.7
CC (mask)	0.87	0.87	0.74	0.55	0.43	0.60
CC (main chain)	0.85	0.85	0.71	0.49	0.48	0.54
CC (side chain)	0.86	0.86	0.75	0.60	0.43	0.66
Average B factors ($Å^2$)						
Protein	79.36	87.85	53.97	72.44	61.69	108.72
Nucleotides	91.66	66.40		47.19		84.41
R.M.S deviations						
Bond lengths (Å)	0.005	0.006	0.013	0.009	0.007	0.007
Bond angles (°)	0.970	1.118	1.466	1.614	1.531	1.367
Validation						
Molprobity score	1.87	1.87	1.90	2.56	1.71	2.12
Clashscore, all atoms	4.26	3.61	6.80	9.58	5.29	7.26
Rotamers outliers (%)	3.26	2.92	0.40	6.67	0.00	2.37
Cβ outliers (%)	0.00	0.00	0.00	0.00	0.00	0.00
CaBLAM outliers (%)	2.01	3.11	4.48	2.56	4.67	3.30
Ramachandran plot						
Favored (%)	95.98	93.98	90.70	93.38	93.50	93.29
Allowed (%)	3.93	5.28	9.18	6.09	5.81	6.49
Outliers (%)	0.090	0.00	0.11	0.53	0.69	0.23

Table S2: Protein-protein and protein-rRNA interaction table.

Protein 1/rRNA		Protein 2/rRNA	
eIF3a	Q6	E78	eS1
	N10	E78	
	R14-a	E78	
	R14-b	D77	
	K23	S192	
eIF3a	Q6	A61	eS26
	R7	D60	
eIF3a	K63	C1116	18S rRNA/ES7^{S}
eIF3a	E135	H465	eIF3c
	T137	Q467	
	R140	Q467	
	R140	P464	
	R140	H465	
	R143	D463	
	S286	L727	
	D343	K745	
	D345	R719	
	R469	D748	
	R476	T794	
	R483	D800	
	R483	V798	
	I484	V798	
	H486	S801	
	H486	S803	
	T487	S801	
	R489	S803	
eIF3a	N399	R317	eIF3m
	I446	K324	
	Q448	K324	
	S449	K324	
	S449	D326	
	E517	K331	
eIF3c	K432	G928	18S rRNA
	K343	G929	
eIF3c	R340	S60	eS27
	L389	E75	
	D602	Y41	
eIF3c	T583	Q283	eIF3e
	R586	V280	
	R586	E284	
	R586	E284	
	D587	N244	
	S834	I347	
	D834	Q349	
	D836	Q349	
eIF3d-NTT	A41	T609	eIF3c
	A43	N610	
	D44	R641	
	W45	Q606	
	T46	R641	
	Q68	N597	
	Y69	T566	
	A70	D562	
	Y71	T566	
	H73	H600	
eIF3g-RRM	N245	T55	uS3
	H307	A88	
	H307	L86	
	I309	A88	
eIF3b	Q553	H156	uS4
	F510	G118	
	V556	K155	
	R505	K155	
	R507	I157	
	R492	G166	
eIF3c-NTD	N131	G1732	18S rRNA
	K123	U1730	
	S139	U367-368	
	Q143	U367	
	R146	U393	

Table S3. Summary of fluorescent data and Kd values for eIF4A binding to eIF3.

[a]Equilibrium dissociation constants determined by titration with eIF3 under the experimental condition.

[b]Anisotropy of the fluorescent labeled molecule prior to addition of eIF3 under the experimental condition.

[c]Calculated anisotropy of the fluorescent labeled molecule in the eIF3 bound state under the experimental condition.

[d]Difference between rfree and rbound, representing the maximum anisotropy change under the experimental condition.

	K_d (nM)[a]	r_{free}[b]	r_{bound}[c]	Δr_{max}[d]
eIF3	~400[e]	0.146 ± 0.001	0.187 ± 0.002	0.041 ± 0.002
eIF3+eIF4G	126 ± 9	0.168 ± 0.0001	0.186 ± 0.0003	0.017 ± 0.0002

Movie S1: Key features of the human 48S translation initiation complex.

References and Notes

1. J. A. Grifo, S. M. Tahara, M. A. Morgan, A. J. Shatkin, W. C. Merrick, New initiation factor activity required for globin mRNA translation. *J. Biol. Chem.* **258**, 5804–5810 (1983). Medline

2. S. Morino, H. Imataka, Y. V. Svitkin, T. V. Pestova, N. Sonenberg, Eukaryotic translation initiation factor 4E (eIF4E) binding site and the middle one-third of eIF4GI constitute the core domain for cap-dependent translation, and the C-terminal one-third functions as a modulatory region. *Mol. Cell. Biol.* **20**, 468–477 (2000). doi:10.1128/MCB.20.2.468-477.2000 Medline

3. A. Marintchev, K. A. Edmonds, B. Marintcheva, E. Hendrickson, M. Oberer, C. Suzuki, B. Herdy, N. Sonenberg, G. Wagner, Topology and regulation of the human eIF4A/4G/4H helicase complex in translation initiation. *Cell* **136**, 447–460 (2009). doi:10.1016/j.cell.2009.01.014 Medline

4. N. Villa, A. Do, J. W. B. Hershey, C. S. Fraser, Human eukaryotic initiation factor 4G (eIF4G) protein binds to eIF3c, -d, and -e to promote mRNA recruitment to the ribosome. *J. Biol. Chem.* **288**, 32932–32940 (2013). doi:10.1074/jbc.M113.517011 Medline

5. A. K. LeFebvre, N. L. Korneeva, M. Trutschl, U. Cvek, R. D. Duzan, C. A. Bradley, J. W. B. Hershey, R. E. Rhoads, Translation initiation factor eIF4G-1 binds to eIF3 through the eIF3e subunit. *J. Biol. Chem.* **281**, 22917–22932 (2006). doi:10.1074/jbc.M605418200 Medline

6. P. Kumar, C. U. T. Hellen, T. V. Pestova, Toward the mechanism of eIF4F-mediated ribosomal attachment to mammalian capped mRNAs. *Genes Dev.* **30**, 1573–1588 (2016). doi:10.1101/gad.282418.116 Medline

7. E. Obayashi, R. E. Luna, T. Nagata, P. Martin-Marcos, H. Hiraishi, C. R. Singh, J. P. Erzberger, F. Zhang, H. Arthanari, J. Morris, R. Pellarin, C. Moore, I. Harmon, E. Papadopoulos, H. Yoshida, M. L. Nasr, S. Unzai, B. Thompson, E. Aube, S. Hustak, F. Stengel, E. Dagraca, A. Ananbandam, P. Gao, T. Urano, A. G. Hinnebusch, G. Wagner, K. Asano, Molecular landscape of the ribosome pre-initiation complex during mRNA scanning: Structural role for eIF3c and its control by eIF5. *Cell Rep.* **18**, 2651–2663 (2017). doi:10.1016/j.celrep.2017.02.052 Medline

8. L. Valášek, K. H. Nielsen, F. Zhang, C. A. Fekete, A. G. Hinnebusch, Interactions of eukaryotic translation initiation factor 3 (eIF3) subunit NIP1/c with eIF1 and eIF5 promote preinitiation complex assembly and regulate start codon selection. *Mol. Cell. Biol.* **24**, 9437–9455 (2004). doi:10.1128/MCB.24.21.9437-9455.2004 Medline

9. V. G. Kolupaeva, A. Unbehaun, I. B. Lomakin, C. U. T. Hellen, T. V. Pestova, Binding of eukaryotic initiation factor 3 to ribosomal 40S subunits and its role in ribosomal dissociation and anti-association. *RNA* **11**, 470–486 (2005). doi:10.1261/rna.7215305 Medline

10. A. des Georges, V. Dhote, L. Kuhn, C. U. T. Hellen, T. V. Pestova, J. Frank, Y. Hashem, Structure of mammalian eIF3 in the context of the 43S preinitiation complex. *Nature* **525**, 491–495 (2015). doi:10.1038/nature14891 Medline

11. D. Andreev, V. Hauryliuk, I. Terenin, S. Dmitriev, M. Ehrenberg, I. Shatsky, The bacterial toxin RelE induces specific mRNA cleavage in the A site of the eukaryote ribosome. *RNA* **14**, 233–239 (2008). doi:10.1261/rna.693208 Medline

12. M. Sokabe, C. S. Fraser, A helicase-independent activity of eIF4A in promoting mRNA recruitment to the human ribosome. *Proc. Natl. Acad. Sci. U.S.A.* **114**, 6304–6309 (2017). doi:10.1073/pnas.1620426114 Medline

13. R. Toribio, I. Díaz-López, J. Boskovic, I. Ventoso, Translation initiation of alphavirus mRNA reveals new insights into the topology of the 48S initiation complex. *Nucleic Acids Res.* **46**, 4176–4187 (2018). doi:10.1093/nar/gky071 Medline

14. J. L. Llácer, T. Hussain, L. Marler, C. E. Aitken, A. Thakur, J. R. Lorsch, A. G. Hinnebusch, V. Ramakrishnan, Conformational Differences between Open and Closed States of the Eukaryotic Translation Initiation Complex. *Mol. Cell* **59**, 399–412 (2015). doi:10.1016/j.molcel.2015.06.033 Medline

15. T. Hussain, J. L. Llácer, I. S. Fernández, A. Munoz, P. Martin-Marcos, C. G. Savva, J. R. Lorsch, A. G. Hinnebusch, V. Ramakrishnan, Structural changes enable start codon recognition by the eukaryotic translation initiation complex. *Cell* **159**, 597–607 (2014). doi:10.1016/j.cell.2014.10.001 Medline

16. T. Hussain, J. L. Llácer, B. T. Wimberly, J. S. Kieft, V. Ramakrishnan, Large-Scale Movements of IF3 and tRNA during Bacterial Translation Initiation. *Cell* **167**, 133–144.e13 (2016). doi:10.1016/j.cell.2016.08.074 Medline

17. C. E. Aitken, P. Beznosková, V. Vlčkova, W.-L. Chiu, F. Zhou, L. S. Valášek, A. G. Hinnebusch, J. R. Lorsch, Eukaryotic translation initiation factor 3 plays distinct roles at the mRNA entry and exit channels of the ribosomal preinitiation complex. *eLife* **5**, e20934 (2016). doi:10.7554/eLife.20934 Medline

18. C. Sun, J. Querol-Audí, S. A. Mortimer, E. Arias-Palomo, J. A. Doudna, E. Nogales, J. H. D. Cate, Two RNA-binding motifs in eIF3 direct HCV IRES-dependent translation. *Nucleic Acids Res.* **41**, 7512–7521 (2013). doi:10.1093/nar/gkt510 Medline

19. J. P. Erzberger, F. Stengel, R. Pellarin, S. Zhang, T. Schaefer, C. H. S. Aylett, P. Cimermančič, D. Boehringer, A. Sali, R. Aebersold, N. Ban, Molecular architecture of the 40S·eIF1·eIF3 translation initiation complex. *Cell* **158**, 1123–1135 (2014). doi:10.1016/j.cell.2014.07.044 Medline

20. A. Simonetti, E. Guca, A. Bochler, L. Kuhn, Y. Hashem, Structural Insights into the Mammalian Late-Stage Initiation Complexes. *Cell Rep.* **31**, 107497 (2020). doi:10.1016/j.celrep.2020.03.061 Medline

21. M. D. Smith, L. Arake-Tacca, A. Nitido, E. Montabana, A. Park, J. H. Cate, Assembly of eIF3 Mediated by Mutually Dependent Subunit Insertion. *Structure* **24**, 886–896 (2016). doi:10.1016/j.str.2016.02.024 Medline

22. L. Cuchalová, T. Kouba, A. Herrmannová, I. Dányi, W.-L. Chiu, L. Valásek, The RNA recognition motif of eukaryotic translation initiation factor 3g (eIF3g) is required for resumption of scanning of posttermination ribosomes for reinitiation on GCN4 and together with eIF3i stimulates linear scanning. *Mol. Cell. Biol.* **30**, 4671–4686 (2010). doi:10.1128/MCB.00430-10 Medline

23. B. Eliseev, L. Yeramala, A. Leitner, M. Karuppasamy, E. Raimondeau, K. Huard, E. Alkalaeva, R. Aebersold, C. Schaffitzel, Structure of a human cap-dependent 48S translation pre-initiation complex. *Nucleic Acids Res.* **46**, 2678–2689 (2018). doi:10.1093/nar/gky054 Medline

24. C. S. Fraser, K. E. Berry, J. W. B. Hershey, J. A. Doudna, eIF3j is located in the decoding center of the human 40S ribosomal subunit. *Mol. Cell* **26**, 811–819 (2007). doi:10.1016/j.molcel.2007.05.019 Medline

25. C. H. S. Aylett, D. Boehringer, J. P. Erzberger, T. Schaefer, N. Ban, Structure of a yeast 40S-eIF1-eIF1A-eIF3-eIF3j initiation complex. *Nat. Struct. Mol. Biol.* **22**, 269–271 (2015). doi:10.1038/nsmb.2963 Medline

26. L. ElAntak, S. Wagner, A. Herrmannová, M. Karásková, E. Rutkai, P. J. Lukavsky, L. Valásek, The indispensable N-terminal half of eIF3j/HCR1 cooperates with its structurally conserved binding partner eIF3b/PRT1-RRM and with eIF1A in stringent AUG selection. *J. Mol. Biol.* **396**, 1097–1116 (2010). doi:10.1016/j.jmb.2009.12.047 Medline

27. V. P. Pisareva, A. V. Pisarev, DHX29 and eIF3 cooperate in ribosomal scanning on structured mRNAs during translation initiation. *RNA* **22**, 1859–1870 (2016). doi:10.1261/rna.057851.116 Medline

28. G. Gouridis, B. Hetzert, K. Kiosze-Becker, M. de Boer, H. Heinemann, E. Nürenberg-Goloub, T. Cordes, R. Tampé, ABCE1 Controls Ribosome Recycling by an Asymmetric Dynamic Conformational Equilibrium. *Cell Rep.* **28**, 723–734.e6 (2019). doi:10.1016/j.celrep.2019.06.052 Medline

29. A. Heuer, M. Gerovac, C. Schmidt, S. Trowitzsch, A. Preis, P. Kötter, O. Berninghausen, T. Becker, R. Beckmann, R. Tampé, Structure of the 40S-ABCE1 post-splitting complex in ribosome recycling and translation initiation. *Nat. Struct. Mol. Biol.* **24**, 453–460 (2017). doi:10.1038/nsmb.3396 Medline

30. D. J. Young, N. R. Guydosh, Hcr1/eIF3j Is a 60S Ribosomal Subunit Recycling Accessory Factor In Vivo. *Cell Rep.* **28**, 39–50.e4 (2019). doi:10.1016/j.celrep.2019.05.111 Medline

31. P. Schütz, M. Bumann, A. E. Oberholzer, C. Bieniossek, H. Trachsel, M. Altmann, U. Baumann, Crystal structure of the yeast eIF4A-eIF4G complex: An RNA-helicase controlled by protein-protein interactions. *Proc. Natl. Acad. Sci. U.S.A.* **105**, 9564–9569 (2008). doi:10.1073/pnas.0800418105 Medline

32. P. Yourik, C. E. Aitken, F. Zhou, N. Gupta, A. G. Hinnebusch, J. R. Lorsch, Yeast eIF4A enhances recruitment of mRNAs regardless of their structural complexity. *eLife* **6**, e31476 (2017). 10.7554/eLife.31476 Medline

33. C. Chapat, S. M. Jafarnejad, E. Matta-Camacho, G. G. Hesketh, I. A. Gelbart, J. Attig, C. G. Gkogkas, T. Alain, N. Stern-Ginossar, M. R. Fabian, A.-C. Gingras, T. F. Duchaine, N. Sonenberg, Cap-binding protein 4EHP effects translation silencing by microRNAs. *Proc. Natl. Acad. Sci. U.S.A.* **114**, 5425–5430 (2017). doi:10.1073/pnas.1701488114 Medline

34. D. J. Cattie, C. E. Richardson, K. C. Reddy, E. M. Ness-Cohn, R. Droste, M. K. Thompson, W. V. Gilbert, D. H. Kim, Mutations in Nonessential eIF3k and eIF3l Genes Confer

Lifespan Extension and Enhanced Resistance to ER Stress in Caenorhabditis elegans. *PLOS Genet.* **12**, e1006326 (2016). doi:10.1371/journal.pgen.1006326 Medline

35. M. D. Smith, Y. Gu, J. Querol-Audí, J. M. Vogan, A. Nitido, J. H. D. Cate, Human-like eukaryotic translation initiation factor 3 from Neurospora crassa. *PLOS ONE* **8**, e78715 (2013). doi:10.1371/journal.pone.0078715 Medline

36. S. K. Archer, N. E. Shirokikh, T. H. Beilharz, T. Preiss, Dynamics of ribosome scanning and recycling revealed by translation complex profiling. *Nature* **535**, 570–574 (2016). doi:10.1038/nature18647 Medline

37. J. Bohlen, K. Fenzl, G. Kramer, B. Bukau, A. A. Teleman, Selective 40S Footprinting Reveals Cap-Tethered Ribosome Scanning in Human Cells. *Mol. Cell* 10.1016/j.molcel.2020.06.005 (2020). doi:10.1016/j.molcel.2020.06.005 Medline

38. Y. Yang, X. Fan, M. Mao, X. Song, P. Wu, Y. Zhang, Y. Jin, Y. Yang, L.-L. Chen, Y. Wang, C. C. Wong, X. Xiao, Z. Wang, Extensive translation of circular RNAs driven by N^6-methyladenosine. *Cell Res.* **27**, 626–641 (2017). doi:10.1038/cr.2017.31 Medline

39. S. E. Wells, P. E. Hillner, R. D. Vale, A. B. Sachs, Circularization of mRNA by eukaryotic translation initiation factors. *Mol. Cell* **2**, 135–140 (1998). doi:10.1016/S1097-2765(00)80122-7 Medline

40. M. Kozak, A short leader sequence impairs the fidelity of initiation by eukaryotic ribosomes. *Gene Expr.* **1**, 111–115 (1991). Medline

41. K. Leppek, R. Das, M. Barna, Functional 5′ UTR mRNA structures in eukaryotic translation regulation and how to find them. *Nat. Rev. Mol. Cell Biol.* **19**, 158–174 (2018). doi:10.1038/nrm.2017.103 Medline

42. A. S. Spirin, How does a scanning ribosomal particle move along the 5′-untranslated region of eukaryotic mRNA? Brownian Ratchet model. *Biochemistry* **48**, 10688–10692 (2009). doi:10.1021/bi901379a Medline

43. C. García-García, K. L. Frieda, K. Feoktistova, C. S. Fraser, S. M. Block, RNA BIOCHEMISTRY. Factor-dependent processivity in human eIF4A DEAD-box helicase. *Science* **348**, 1486–1488 (2015). doi:10.1126/science.aaa5089 Medline

44. F. Rozen, I. Edery, K. Meerovitch, T. E. Dever, W. C. Merrick, N. Sonenberg, Bidirectional RNA helicase activity of eucaryotic translation initiation factors 4A and 4F. *Mol. Cell. Biol.* **10**, 1134–1144 (1990). doi:10.1128/MCB.10.3.1134 Medline

45. S. Takyar, R. P. Hickerson, H. F. Noller, mRNA helicase activity of the ribosome. *Cell* **120**, 49–58 (2005). doi:10.1016/j.cell.2004.11.042 Medline

46. D. Tauber, G. Tauber, A. Khong, B. Van Treeck, J. Pelletier, R. Parker, Modulation of RNA Condensation by the DEAD-Box Protein eIF4A. *Cell* **180**, 411–426.e16 (2020). doi:10.1016/j.cell.2019.12.031 Medline

47. K. Feoktistova, E. Tuvshintogs, A. Do, C. S. Fraser, Human eIF4E promotes mRNA restructuring by stimulating eIF4A helicase activity. *Proc. Natl. Acad. Sci. U.S.A.* **110**, 13339–13344 (2013). doi:10.1073/pnas.1303781110 Medline

48. S. V. Slepenkov, N. L. Korneeva, R. E. Rhoads, Kinetic mechanism for assembly of the m7GpppG.eIF4E.eIF4G complex. *J. Biol. Chem.* **283**, 25227–25237 (2008). doi:10.1074/jbc.M801786200 Medline

49. A. S. Lee, P. J. Kranzusch, J. A. Doudna, J. H. D. Cate, eIF3d is an mRNA cap-binding protein that is required for specialized translation initiation. *Nature* **536**, 96–99 (2016). doi:10.1038/nature18954 Medline

50. M. Sokabe, C. S. Fraser, Human eukaryotic initiation factor 2 (eIF2)-GTP-Met-tRNAi ternary complex and eIF3 stabilize the 43 S preinitiation complex. *J. Biol. Chem.* **289**, 31827–31836 (2014). doi:10.1074/jbc.M114.602870 Medline

51. M. A. Griffin, J. H. Davis, S. A. Strobel, Bacterial toxin RelE: A highly efficient ribonuclease with exquisite substrate specificity using atypical catalytic residues. *Biochemistry* **52**, 8633–8642 (2013). doi:10.1021/bi401325c Medline

52. J. Brito Querido, E. Mancera-Martínez, Q. Vicens, A. Bochler, J. Chicher, A. Simonetti, Y. Hashem, The cryo-EM Structure of a Novel 40S Kinetoplastid-Specific Ribosomal Protein. *Structure* **25**, 1785–1794.e3 (2017). doi:10.1016/j.str.2017.09.014 Medline

53. M. Götze, J. Pettelkau, R. Fritzsche, C. H. Ihling, M. Schäfer, A. Sinz, Automated assignment of MS/MS cleavable cross-links in protein 3D-structure analysis. *J. Am. Soc. Mass Spectrom.* **26**, 83–97 (2015). doi:10.1007/s13361-014-1001-1 Medline

54. C. J. Russo, S. Scotcher, M. Kyte, A precision cryostat design for manual and semi-automated cryo-plunge instruments. *Rev. Sci. Instrum.* **87**, 114302 (2016). doi:10.1063/1.4967864 Medline

55. J. Zivanov, T. Nakane, B. O. Forsberg, D. Kimanius, W. J. Hagen, E. Lindahl, S. H. Scheres, New tools for automated high-resolution cryo-EM structure determination in RELION-3. *eLife* **7**, e42166 (2018). doi:10.7554/eLife.42166 Medline

56. A. Rohou, N. Grigorieff, CTFFIND4: Fast and accurate defocus estimation from electron micrographs. *J. Struct. Biol.* **192**, 216–221 (2015). doi:10.1016/j.jsb.2015.08.008 Medline

57. I. B. Lomakin, T. A. Steitz, The initiation of mammalian protein synthesis and mRNA scanning mechanism. *Nature* **500**, 307–311 (2013). doi:10.1038/nature12355 Medline

58. T. Nakane, D. Kimanius, E. Lindahl, S. H. Scheres, Characterisation of molecular motions in cryo-EM single-particle data by multi-body refinement in RELION. *eLife* **7**, e36861 (2018). doi:10.7554/eLife.36861 Medline

59. S. Chen, G. McMullan, A. R. Faruqi, G. N. Murshudov, J. M. Short, S. H. W. Scheres, R. Henderson, High-resolution noise substitution to measure overfitting and validate resolution in 3D structure determination by single particle electron cryomicroscopy. *Ultramicroscopy* **135**, 24–35 (2013). doi:10.1016/j.ultramic.2013.06.004 Medline

60. A. Waterhouse, M. Bertoni, S. Bienert, G. Studer, G. Tauriello, R. Gumienny, F. T. Heer, T. A. P. de Beer, C. Rempfer, L. Bordoli, R. Lepore, T. Schwede, SWISS-MODEL: Homology modelling of protein structures and complexes. *Nucleic Acids Res.* **46**, W296–W303 (2018). doi:10.1093/nar/gky427 Medline

61. Z. Wei, P. Zhang, Z. Zhou, Z. Cheng, M. Wan, W. Gong, Crystal structure of human eIF3k, the first structure of eIF3 subunits. *J. Biol. Chem.* **279**, 34983–34990 (2004). doi:10.1074/jbc.M405158200 Medline

62. J. L. Llácer, T. Hussain, A. K. Saini, J. S. Nanda, S. Kaur, Y. Gordiyenko, R. Kumar, A. G. Hinnebusch, J. R. Lorsch, V. Ramakrishnan, Translational initiation factor eIF5 replaces eIF1 on the 40S ribosomal subunit to promote start-codon recognition. *eLife* **7**, e39273 (2018). doi:10.7554/eLife.39273 Medline

63. E. Schmitt, M. Panvert, C. Lazennec-Schurdevin, P.-D. Coureux, J. Perez, A. Thompson, Y. Mechulam, Structure of the ternary initiation complex aIF2-GDPNP-methionylated initiator tRNA. *Nat. Struct. Mol. Biol.* **19**, 450–454 (2012). doi:10.1038/nsmb.2259 Medline

64. D. T. Jones, Protein secondary structure prediction based on position-specific scoring matrices. *J. Mol. Biol.* **292**, 195–202 (1999). doi:10.1006/jmbi.1999.3091 Medline

65. S. K. Natchiar, A. G. Myasnikov, H. Kratzat, I. Hazemann, B. P. Klaholz, Visualization of chemical modifications in the human 80S ribosome structure. *Nature* **551**, 472–477 (2017). doi:10.1038/nature24482 Medline

66. A. Casañal, B. Lohkamp, P. Emsley, Current Developments in Coot for Macromolecular Model Building of Electron Cryo-microscopy and Crystallographic Data. *Protein Sci.* **29**, 1055–1064 (2020). doi:10.1002/pro.3791 Medline

67. P. V. Afonine, B. K. Poon, R. J. Read, O. V. Sobolev, T. C. Terwilliger, A. Urzhumtsev, P. D. Adams, Real-space refinement in PHENIX for cryo-EM and crystallography. *Acta Crystallogr. D* **74**, 531–544 (2018). doi:10.1107/S2059798318006551 Medline

68. L. Zimmermann, A. Stephens, S.-Z. Nam, D. Rau, J. Kübler, M. Lozajic, F. Gabler, J. Söding, A. N. Lupas, V. Alva, A Completely Reimplemented MPI Bioinformatics Toolkit with a New HHpred Server at its Core. *J. Mol. Biol.* **430**, 2237–2243 (2018). doi:10.1016/j.jmb.2017.12.007 Medline

69. E. F. Pettersen, T. D. Goddard, C. C. Huang, G. S. Couch, D. M. Greenblatt, E. C. Meng, T. E. Ferrin, UCSF Chimera—A visualization system for exploratory research and analysis. *J. Comput. Chem.* **25**, 1605–1612 (2004). doi:10.1002/jcc.20084 Medline

70. T. D. Goddard, C. C. Huang, E. C. Meng, E. F. Pettersen, G. S. Couch, J. H. Morris, T. E. Ferrin, UCSF ChimeraX: Meeting modern challenges in visualization and analysis. *Protein Sci.* **27**, 14–25 (2018). doi:10.1002/pro.3235 Medline

71. T. Becker, S. Franckenberg, S. Wickles, C. J. Shoemaker, A. M. Anger, J.-P. Armache, H. Sieber, C. Ungewickell, O. Berninghausen, I. Daberkow, A. Karcher, M. Thomm, K.-P. Hopfner, R. Green, R. Beckmann, Structural basis of highly conserved ribosome recycling in eukaryotes and archaea. *Nature* **482**, 501–506 (2012). doi:10.1038/nature10829 Medline

72. A. Brown, S. Shao, J. Murray, R. S. Hegde, V. Ramakrishnan, Structural basis for stop codon recognition in eukaryotes. *Nature* **524**, 493–496 (2015). doi:10.1038/nature14896 Medline

73. S. Grüner, D. Peter, R. Weber, L. Wohlbold, M.-Y. Chung, O. Weichenrieder, E. Valkov, C. Igreja, E. Izaurralde, The Structures of eIF4E-eIF4G Complexes Reveal an Extended Interface to Regulate Translation Initiation. *Mol. Cell* **64**, 467–479 (2016). doi:10.1016/j.molcel.2016.09.020 Medline